The Astrophysical Journal, 715:1400–1407, 2010 June 1 doi:10.1088/0004-637X/715/2/1400

MEASUREMENTS OF THE RELATIVE ABUNDANCES OF HIGH-ENERGY COSMIC-RAY NUCLEI IN THE TeV/NUCLEON REGION

H. S. Ahn[1], P. S. Allison[2], M. G. Bagliesi[3], L. Barbier[4], J. J. Beatty[2], G. Bigongiari[3], T. J. Brandt[2], J. T. Childers[5], N. B. Conklin[6], S. Coutu[6], M. A. DuVernois[5], O. Ganel[1], J. H. Han[1], J. A. Jeon[7], K. C. Kim[1], J. Lee[7], M. H. Lee[1], P. Maestro[3], A. Malinin[1], P. S. Marrocchesi[3], S. Minnick[8], S. I. Mognet[6], G. W. Na[7], J. Nam[7], S. Nam[7], S. Nutter[9], I. H. Park[7,11], N. H. Park[7], E. S. Seo[1,10], R. Sina[1], P. Walpole[1], J. Wu[1], J. Yang[7], Y. S. Yoon[1,2], R. Zei[3], and S. Y. Zinn[1]
[1] Institute for Physical Science and Technology, University of Maryland, College Park, MD 20742, USA
[2] Department of Physics, Ohio State University, Columbus, OH 43210, USA
[3] Department of Physics, University of Siena & INFN, Via Roma 56, 53100 Siena, Italy
[4] Astroparticle Physics Laboratory, NASA Goddard Space Flight Center, Greenbelt, MD 20771, USA
[5] School of Physics and Astronomy, University of Minnesota, Minneapolis, MN 55455, USA
[6] Department of Physics, Penn State University, University Park, PA 16802, USA
[7] Department of Physics, Ewha Womans University, Seoul 120-750, Republic of Korea
[8] Department of Physics, Kent State University, Tuscarawas, New Philadelphia, OH 44663, USA
[9] Department of Physics and Geology, Northern Kentucky University, Highland Heights, KY 41099, USA
[10] Department of Physics, University of Maryland, College Park, MD 20742, USA
Received 2009 July 20; accepted 2010 April 12; published 2010 May 11

ABSTRACT

We present measurements of the relative abundances of cosmic-ray nuclei in the energy range of 500–3980 GeV/nucleon from the second flight of the Cosmic Ray Energetics And Mass balloon-borne experiment. Particle energy was determined using a sampling tungsten/scintillating-fiber calorimeter, while particle charge was identified precisely with a dual-layer silicon charge detector installed for this flight. The resulting element ratios C/O, N/O, Ne/O, Mg/O, Si/O, and Fe/O at the top of atmosphere are $0.919 \pm 0.123^{\rm stat} \pm 0.030^{\rm syst}$, $0.076 \pm 0.019^{\rm stat} \pm 0.013^{\rm syst}$, $0.115 \pm 0.031^{\rm stat} \pm 0.004^{\rm syst}$, $0.153 \pm 0.039^{\rm stat} \pm 0.005^{\rm syst}$, $0.180 \pm 0.045^{\rm stat} \pm 0.006^{\rm syst}$, and $0.139 \pm 0.043^{\rm stat} \pm 0.005^{\rm syst}$, respectively, which agree with measurements at lower energies. The source abundance of N/O is found to be $0.054 \pm 0.013^{\rm stat} \pm 0.009^{\rm syst+0.010esc}_{-0.017}$. The cosmic-ray source abundances are compared to local Galactic (LG) abundances as a function of first ionization potential and as a function of condensation temperature. At high energies the trend that the cosmic-ray source abundances at large ionization potential or low condensation temperature are suppressed compared to their LG abundances continues. Therefore, the injection mechanism must be the same at TeV/nucleon energies as at the lower energies measured by HEAO-3, CRN, and TRACER. Furthermore, the cosmic-ray source abundances are compared to a mixture of 80% solar system abundances and 20% massive stellar outflow (MSO) as a function of atomic mass. The good agreement with TIGER measurements at lower energies confirms the existence of a substantial fraction of MSO material required in the ∼TeV per nucleon region.

Key words: acceleration of particles – balloons – diffusion – Galaxy: abundances

Online-only material: color figures

1. INTRODUCTION

Chemical abundances of cosmic rays provide an important clue to their origin and propagation from their sources to the Earth. Primary cosmic-ray nuclei may be accelerated by supernovae, while secondary cosmic-ray nuclei are created by spallation processes via nuclear interactions with interstellar gas. Substantial fractions of the common elements carbon, oxygen, neon, magnesium, and silicon traverse the distance between their sources and the Earth without significant interactions. Boron nuclei arriving at the Earth are mostly secondaries. Nitrogen nuclei arriving at the top of the atmosphere are a mixture of primary and secondary nuclei. Correcting for the secondary fraction due to spallation, one can calculate the residual abundance at the source. For a recent review on the importance of secondary nuclei abundances, see Strong et al. (2007).

Relative abundances of cosmic-ray nuclei allow one to study the propagation model of cosmic rays, which must account for changes in energy, diffusion, convection, nuclear interactions, radioactive decay, and spallation processes. High-energy cosmic-ray data are particularly useful, as convection, nuclear decay, and changes in energy are negligible in their propagation. Due to the low flux at high energies, however, few measurements are available above several hundred GeV per nucleon.

The relative abundances of cosmic rays vary with energy. While some variations may be associated with differences in the primary injection spectra, variations of the secondary-to-primary ratio as a function of energy point to a second effect. Previous measurements of the boron-to-carbon (B/C) and subiron-to-iron ratios, clearly showing such energy dependence, suggest that spallation path lengths depend on particle energy or magnetic rigidity (Juliusson et al. 1972; Smith et al. 1973; Swordy et al. 1990; Engelmann et al. 1990). The simplest explanation is that the trajectories of particles of higher rigidity are less affected by interstellar magnetic fields, resulting in shorter paths with increasing rigidity. The energy dependence of the path length for escape from the Galaxy is of the form $X_e(E) = X_0(E/E_0)^{-\delta}$, the escape parameter δ being positive, so that the spallation path length decreases at high energies. From Garcia-Munoz et al. (1987), a dependence of the form $X_e(E) \sim E^{-0.6}$ provides a good fit to experimental observations (e.g., Swordy et al. 1993; Yanasak et al. 2001; Müller et al. 2005). This dependence is consistent with recent observations

[11] Corresponding author: ipark@ewha.ac.kr

by Ahn et al. (2008) of the B/C ratio. The N/O ratio would have less energy dependence because there is an additional primary nitrogen contribution (Swordy et al. 1990). Therefore, because the escape path length decreases with energy, at a high-enough energy there will be only a small contribution from spallation, and the primary nitrogen abundance can be measured with less systematic uncertainty. These variations in path length with energy provide information about the processes of diffusion of high-energy particles in the interstellar medium.

The well-known differences between the Galactic cosmic-ray source (GCRS) abundances and their local Galactic (LG) abundances are believed to be correlated with the atomic properties of the elements. A systematic trend of suppressed abundances relative to LG abundances is seen for elements with first ionization potentials (FIPs) greater than ∼10 eV. On the other hand, source abundances can also be fractionated according to the elements' volatility (Meyer et al. 1997). Cosmic-ray abundances can be ordered by the elements that form the dust grains, implying therefore that refractory elements (generally with low-FIP, such as Mg and Si) locked in grains in the interstellar medium could be more abundant in cosmic rays than volatile elements (generally with high-FIP such as C, N, O, and Ne).

An alternate ordering of elements has been suggested by the TIGER collaboration (Rauch et al. 2009) to differentiate between refractory and volatile elements. It suggests the ordering of elements in terms of the ratio of the GCRS abundances to a mixture of 80% solar system (SS) abundances and 20% massive stellar outflow (MSO) as a function of atomic mass. The study suggests that this ordering provides evidence which supports an OB-association environment model and more effective acceleration of interstellar grains than interstellar gas.

The Cosmic Ray Energetics And Mass (CREAM) balloon-borne experiment was designed for direct measurement of cosmic-ray nuclei in the energy range between 10^{11} eV and 10^{15} eV, from protons to iron nuclei, in a series of long-duration balloon flights (Seo et al. 2008; Ahn et al. 2010). Detailed investigations in this energy range will allow us to understand the mechanisms of particle acceleration, propagation, and confinement. The first flight of CREAM (CREAM-I) was carried out during the 2004/2005 season; it was launched from McMurdo Station, Antarctica. In the following seasons of 2005/2006, 2007/2008, 2008/2009, and 2009/2010 CREAM-II, III, IV, and V were flown, respectively. With five successful flights, a cumulative exposure of nearly 160 days was achieved.

We present relative abundances of cosmic-ray nuclei from carbon to iron at energies up to several TeV per nucleon, as measured by CREAM-II, in which charge measurement was significantly improved compared to CREAM-I with a new dual-layer silicon charge detector (SCD). A complementary analysis on the CREAM-II data is presented in a paper by Ahn et al. (2009).

2. THE CREAM EXPERIMENT

2.1. The CREAM Instrument

The CREAM instrument consists of highly segmented (about 10,000 electronic channels) complementary and redundant particle detectors (Ahn et al. 2007) to measure the charge and energy of high-energy cosmic rays. The instrumental configurations of CREAM-I, II, III, IV, and V differ due to various upgrades. The data for the present analysis were obtained from CREAM-II. As shown in Figure 1, CREAM-II includes a timing charge detector (TCD) consisting of a plastic scintillation assembly, an acrylic Cherenkov detector (CD), a dual-layer SCD, and a sampling tungsten/scintillating-fiber calorimeter (CAL) for energy measurement, preceded by a pair of graphite targets for initiating a shower in the CAL. S3, a single layer of scintillating fibers located between the target and the calorimeter, provides a reference time for the TCD and aids with triggering. Multiple charge measurements by the TCD, CD, and SCD systems allow complementary charge identification. Each detector has its own independent method for minimizing the effect of backscattered particles from the calorimeter, thereby allowing accurate identification of incident particle charges (for more details see Seo et al. 2008).

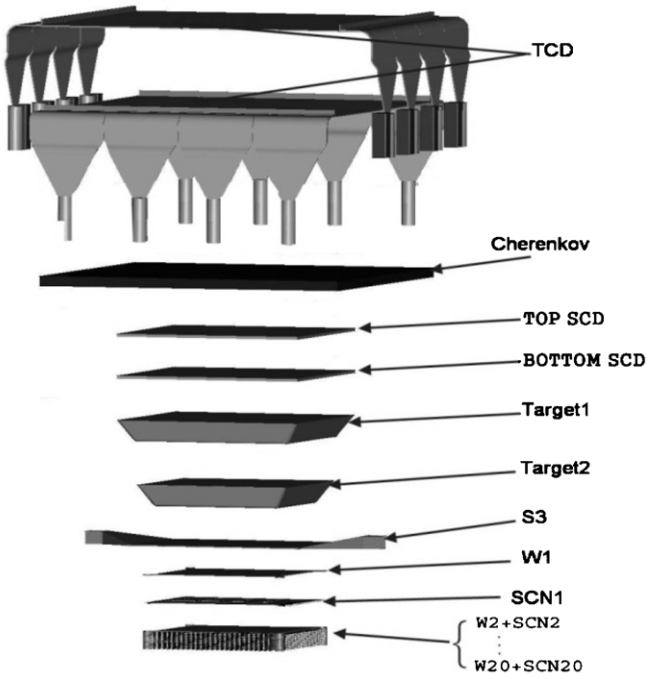

Figure 1. Layout of the CREAM-II instrument.

2.2. The Calorimeter

The CAL measures the energy of the shower produced by hadronic interactions of cosmic rays in the carbon target. It is a sampling calorimeter with 20 layers of tungsten absorber, each one-radiation length thick, interleaved with 20 active layers of scintillating-fiber ribbons. Each active layer is comprised of fifty 1 cm wide ribbons, each made of nineteen 0.5 mm diameter fibers. Active layers alternate orientations between X and Y providing 10 measurements in the X–Z plane and 10 in the Y–Z plane (Marrocchesi et al. 2004).

The CAL provides tracking information that determines the segment(s) of each charge detector traversed by the primary cosmic-ray particle. Incident particle tracks are determined by extrapolating each shower axis back to the charge detectors. The tracking uncertainty is smaller than the pixel size of the SCD.

2.3. The Silicon Charge Detector

The SCD is comprised of an array of DC-type silicon PIN diodes. A cosmic ray passing through the sensor produces ionization in the depleted region. The amount of ionization is proportional to the square of the charge of the incident particle.

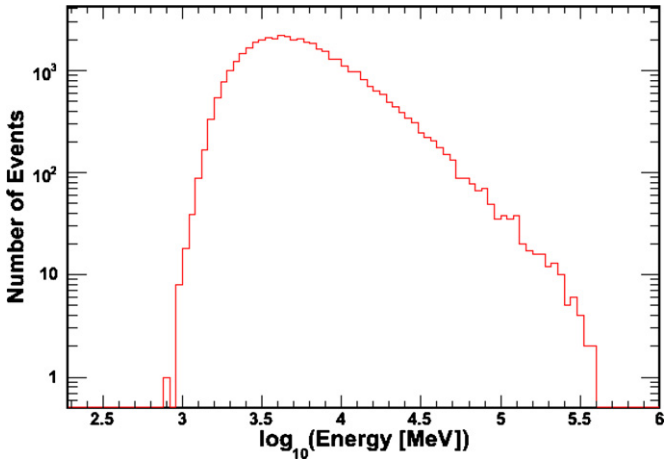

Figure 2. Energy deposited in the calorimeter for events selected by the CAL trigger.

(A color version of this figure is available in the online journal.)

The building block of the SCD is a silicon sensor fabricated on a 5 inch, 380 μm thick wafer. The sensor is segmented into a 4×4 matrix of 16 pixels. The 2.12 cm^2 active area of each pixel is optimized to reduce the effect of backscatter from showers in the calorimeter, while keeping the channel count and power at manageable levels (Park et al. 2006, 2007). For CREAM-II, the single-layer SCD flown in CREAM-I was replaced by a dual-layer SCD with a total of 4992 pixels, significantly improving charge resolution (Nam et al. 2007). The overall SCD thickness is 97.5 mm, including a 21 mm gap between layers.

2.4. Operation

CREAM-II spent 28 days at float with two circumnavigations of the South Pole from 2005 December 16 to 2006 January 13. The balloon's altitude varied between 38 and 40 km through most of the flight, with a corresponding average atmospheric overburden of $\sim$3.9 g cm^{-2}. Diurnal altitude variation due to changes in the Sun's angle was $<$1 km near the South Pole, increasing somewhat as the balloon spiraled outward to lower latitudes later in the flight. Despite the daily variation of a few °C, consistent with the Sun's angle, the temperatures of all instrument systems remained within their operational ranges. High-energy data acquired using the CAL trigger were transmitted via the Tracking and Data Relay Satellite System (TDRSS) during the flight, while lower-energy data were recorded onboard. See Seo et al. (2008) for more details of flight operations and instrument flight performance.

3. DATA ANALYSIS

3.1. Event Selection

In flight, the CAL provided a trigger whenever a significant energy deposit occurred within it. This was accomplished by requiring an energy deposit of more than 60 MeV in at least one ribbon in each of six or more consecutive layers. Such an energy-based trigger becomes fully efficient above an incident energy of near a TeV. Events are first selected on board upon the occurrence of a calorimeter shower during the flight. Figure 2 shows the energy deposition distribution in the calorimeter.

3.2. Energy Measurement

Due to the weight limits imposed by long duration ballooning, calorimeters are thin and thus not able to contain complete hadronic showers. To characterize this, the resulting shower leakage has been studied with both accelerator beams and Monte Carlo simulations. Beam-test data show good agreement with simulations for the energy range available at CERN, up to 350 GeV for protons. Above that limit, simulations indicate that the calorimeter response is nearly linear in the CREAM energy range. The ratio of energy deposit in the calorimeter to the full incident energy was found to be 0.015% for protons. This value is used for energy reconstruction of the incident nucleus. Using this conversion factor, the energy resolution is found to be 45% from the beam test data for carbon, while the average value of 30% for nuclei $Z \geqslant 5$ was quoted in Ahn et al. (2009). The energy resolution is 60% for boron, 45% for carbon, 35% for oxygen, and 22% for iron, for example, and not linear in Z.

3.3. Charge Calibration, Determination, and Correction

The SCD data in this study were carefully examined and calibrated by taking into account variations for each pixel in pedestal, temperature, and gain.

The hit position in the SCD was determined by extrapolating the trajectories reconstructed from the CAL to the SCD. The hadronic shower axis of an incident cosmic ray was determined first in the CAL by using a weighted least-squares fit. Only tracks that had at least six out of 20 layers of CAL activated (three each in the X–Z and Y–Z planes) were selected. Coordinates of active ribbons in the layers were weighted by the ratio of energy deposited in the ribbon to the total energy deposited in the layer. Track quality was assessed using the chi squared value, requiring $\chi^2 < 10$.

The reconstructed track was extrapolated to each of the SCD planes, with the hit area defined by considering the shower reconstruction error. The residual of the extrapolated track position relative to the pixel center position in the top and bottom SCDs is about 1.8 cm and 1.7 cm along the x-axis, and 1.7 cm and 1.6 cm along the y-axis, respectively. To avoid charge misidentification as a result of secondary shower particles, we selected the pixel with the maximal signal out of those pixels within a circle with a 4.5 cm radius centered at the extrapolated track position. A track fit including the SCD hits is made again, which leads to a final residual of 3 mm for both the x- and y-axes.

Energy loss in the silicon depends on the path length of the incident particle traversing the sensor. SCD signals were thus subjected to angle corrections using the reconstructed trajectory information. Charge distributions of the SCD before and after correction for incident angles are shown in Figure 3, illustrating a significant improvement in the charge resolution up to iron.

3.4. Event Sample for Relative Abundance Ratios

Figure 4(a) shows the distribution of charge differences between the top and bottom SCD layers. The charge difference between the top and bottom SCD layers is mainly caused by superposition of backscattered particles, dead channels in one of the two layers, or by the interaction of particles in the material located between the top and bottom layers. A consistency of charge measurements from two SCD layers, $|Z_{\rm top} - Z_{\rm bottom}| < \Delta Z$, is required as shown with dotted lines in Figure 4(b). ΔZ was chosen to be 0.57 for carbon and widened linearly to $\Delta Z = 0.88$ at Fe as Z increases by taking into account the Z-dependent charge resolution.

The average signal of the top and bottom SCD layers is shown in Figure 5 for events passing the charge consistency requirement. The charge resolutions of the SCD for carbon,

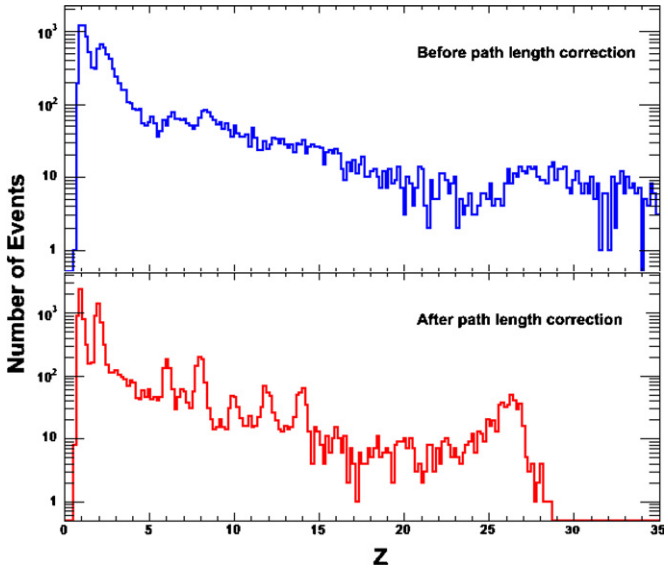

Figure 3. Distribution of charge measured by the SCD before (top) and after (bottom) correction for incident cosmic-ray trajectory angle.
(A color version of this figure is available in the online journal.)

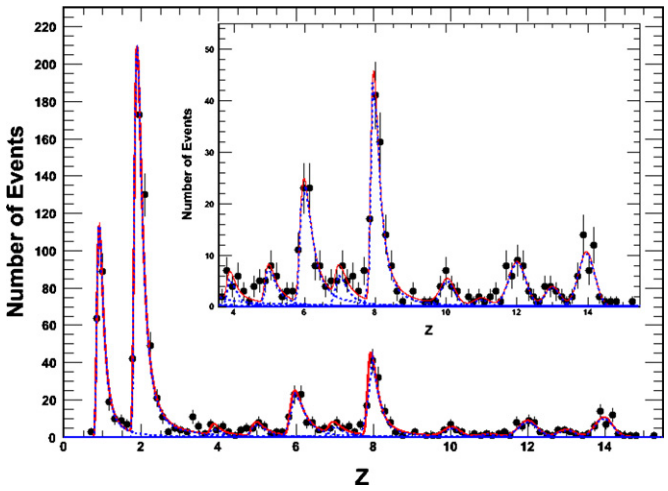

Figure 5. Charge distribution of the events selected using the charge consistency check in the energy range 7.0 TeV $< E <$ 55.7 TeV. Data points are the average of signals from the top and bottom SCD layers after event selection and consistency requirements. The distribution is fitted using multi-Landau (for $Z \leqslant 8$) and multi-Gaussian (for $Z \geqslant 9$) functions. The inner graph shows the distribution for Z greater than 3.
(A color version of this figure is available in the online journal.)

nitrogen, oxygen, neon, magnesium, and silicon range from 0.15 to 0.24, and with a charge-dependent resolution, more accurate at low Z. The Z distribution of proton and helium clearly follows the Landau distribution. It tends to be smeared out as Z increases, but still Landau-like up to oxygen. However, the distribution above oxygen becomes Gaussian-like.

Averaged charge histograms were fitted using multi-Landau (for $Z \leqslant 8$) and multi-Gaussian (for $Z \geqslant 9$) functions. For successful fittings, peak widths of rare elements are fixed by estimated values using neighboring elements. The distributions were well fitted except for lithium, beryllium, and boron, where the number of detected events is not large enough to resolve these species from proton and helium contamination. The number of each charge species is obtained from the area under the fitted functions.

The events selected above are shown in Figure 6 as a function of the energy per nucleon (GeV/nucleon) for the lightest (carbon) and heaviest (iron) elements of the data sample studied here. The cutoff in the distribution below 100 GeV/nucleon is due to the trigger threshold. For each element sample, the energy range of the measurement is chosen to be above 500 GeV/nucleon, where trigger efficiency uncertainty is negligible. The dependence of the Z measurement on energy was also found to be negligible. The energy bins of the measurement were chosen to be much larger than the energy resolution of the calorimeter.

3.5. Corrections for Interaction in the Upper Atmosphere and Detector Material

Secondary particles may be created from the interaction of incident cosmic rays with materials above the SCD, which include both CREAM systems above the SCD and the atmospheric overburden. Data from the selection described above are corrected for this effect. The correction is calculated in two parts: corrections up to the top of the instrument (TOI) and up to the top of the atmosphere (TOA).

The average atmospheric overburden during the CREAM-II flight was measured to be $\sim$3.9 g cm^{-2}. The average atomic mass

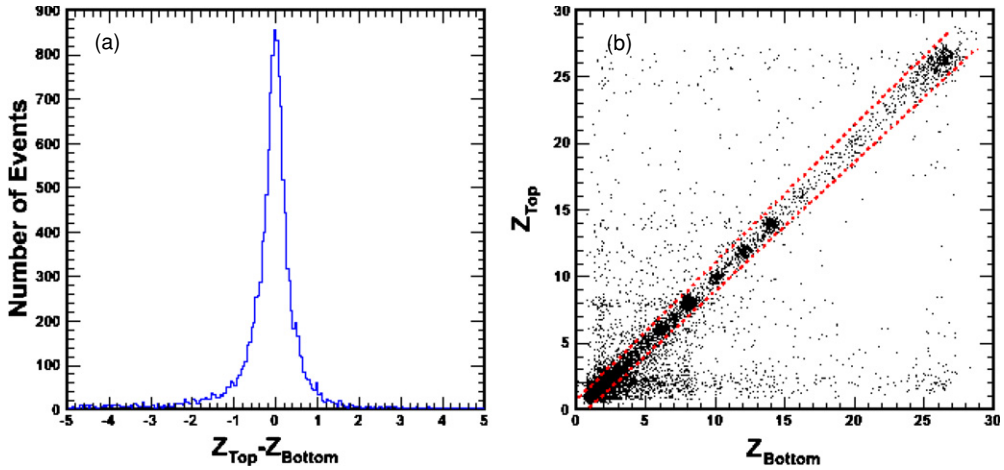

Figure 4. Consistency test of charge measurement from the dual-layer SCD. (a) Charge difference between top SCD and bottom SCD. (b) Top SCD vs. bottom SCD.
(A color version of this figure is available in the online journal.)

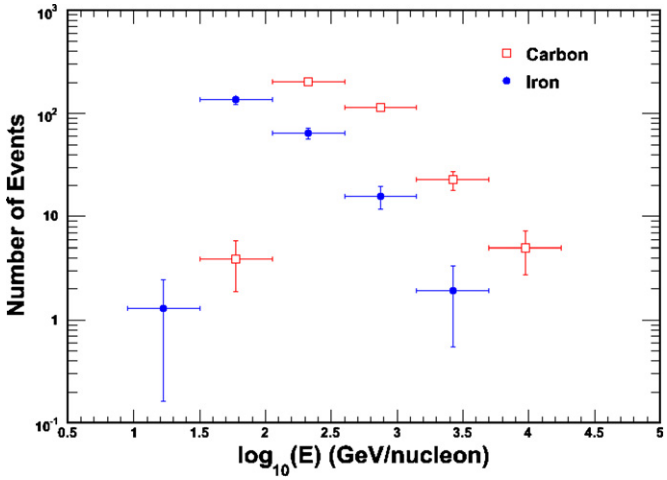

Figure 6. Number of events for carbon ($Z = 6$) and iron ($Z = 26$) as a function of the energy/nucleon.

(A color version of this figure is available in the online journal.)

of the air was estimated by a weighted sum of air composition (78% nitrogen, 21% oxygen, 1% argon). The average atomic mass of materials of CREAM-II systems above the SCD is estimated to be 14.85 amu. The column density of that material is 2.41 g cm^{-2} on average.

Quantities at TOA were estimated using the transport equation given by a weighted-slab model (Ptuskin et al. 1996). Webber's energy-independent empirical formula was employed to estimate the total charge-changing cross sections (Webber et al. 1990). Nucleus–nucleus fragmentation cross sections were calculated from the factorization given by Olson et al. (1983) to the scaling factors of Putze et al. (2008) and proton–nucleus fragmentation cross sections compiled by Silberberg & Tsao (2004). The same method was applied to the correction to TOI.

A transport matrix M was constructed from the above calculation. This takes the form of a 26 × 26 matrix of conversion probabilities during the passage of a given range of material. The transport process is then described by the matrix equation $D = M \times E$, where the elemental distribution at incident level E leads to the measured distribution D. Once the matrix M of each transport step is known, we can apply the inverse matrix to reach the final spectrum of elements step-by-step from the initial detector measurements. That is, the matrix M contains information about nuclear spallation that gives the loss and gain of each element as measured by the detector.

4. RESULTS

4.1. Measurement of Abundance Ratios

After applying the TOI and TOA corrections to the selected data set, the relative abundance ratios of elements are shown in Figure 7, with a filled square denoting the (a) C/O, (b) N/O, (c) Ne/O, (d) Mg/O, (e) Si/O, and (f) Fe/O ratio in each graph, respectively. Previous measurements from CRN (Müller et al. 1991; Swordy et al. 1990) and HEAO (Engelmann et al. 1990) are shown in the figures as open squares and circles, respectively. The values of the ratios are calculated from the absolute fluxes reported by those experiments. The recent measurements from CREAM-I data in a different configuration are shown as filled

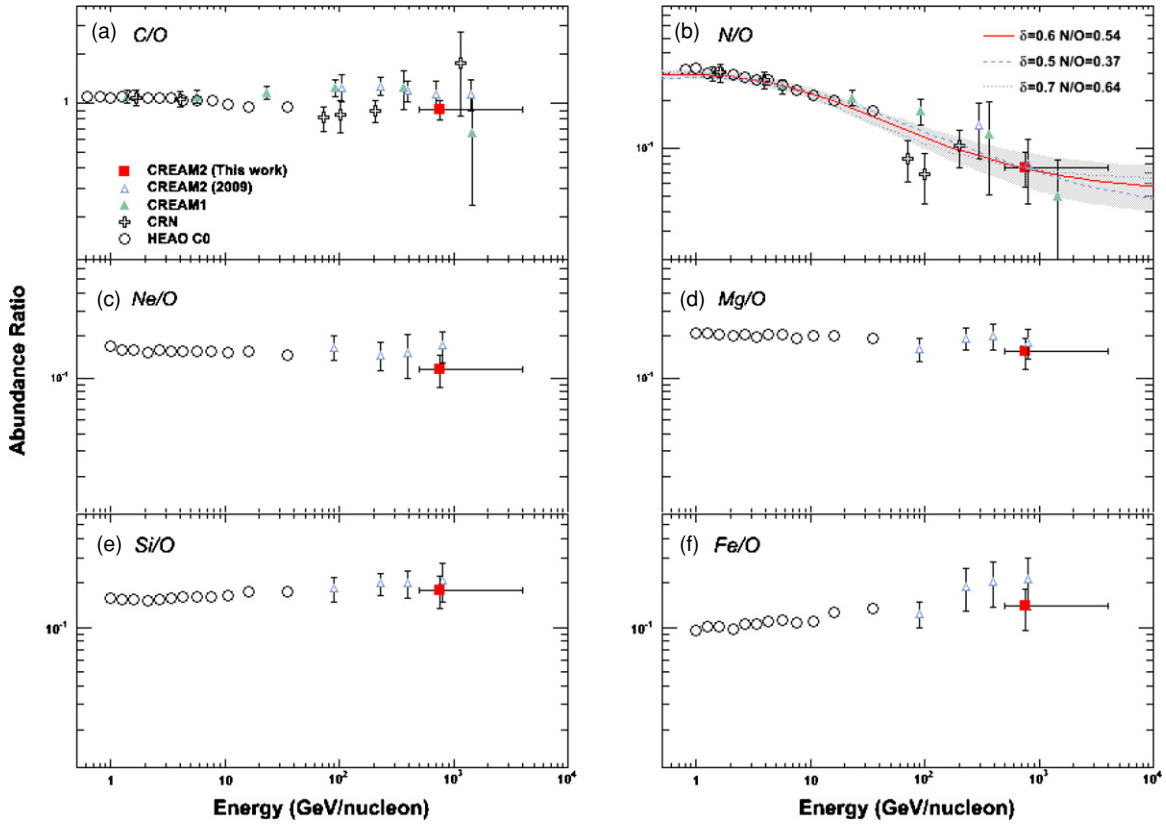

Figure 7. Relative ratios of the elements (a) C/O, (b) N/O, where lines represent the N/O ratio curve calculated by GALPROP (see Section 5), (c) Ne/O, (d) Mg/O, (e) Si/O, and (f) Fe/O.

(A color version of this figure is available in the online journal.)

Table 1
Measured and Corrected Values of C/O, N/O, Ne/O, Mg/O, Si/O, and Fe/O Ratios[a]

Elemental Ratio	Kinetic Energy (GeV/Nucleon)	Observed Ratio	Corrected Ratio ± Statistical Error ± Total Systematic Error	Energy Range (GeV/Nucleon)
C/O	746	1.045 ± 0.140	0.919 ± 0.123 ± 0.030	500–3980
N/O	746	0.182 ± 0.044	0.076 ± 0.019 ± 0.013	500–3980
Ne/O	746	0.149 ± 0.040	0.115 ± 0.031 ± 0.004	500–3980
Mg/O	746	0.167 ± 0.042	0.153 ± 0.039 ± 0.005	500–3980
Si/O	746	0.172 ± 0.043	0.180 ± 0.045 ± 0.006	500–3980
Fe/O	746	0.105 ± 0.033	0.139 ± 0.043 ± 0.005	500–3980

Note. [a] The systematic uncertainty includes uncertainties from charge selection, TOA cross section, TOI cross section, TOA material depth, and TOI material depth.

triangles in the figures (Ahn et al. 2008) and the complementary analysis of CREAM-II data are displayed as open triangles (Ahn et al. 2009).

The uncertainty in the corrected abundance ratios for the CREAM-II data shown in the figure is the quadrature sum of statistical and systematic errors. The measured and corrected numbers together with systematic errors are listed in Table 1. The statistical error is derived by error propagation of each element to a ratio, while the measured number of events is used for the statistical error estimate without the TOI and TOA corrections. The systematic errors are discussed in the following subsection.

4.2. Systematic Checks

Systematic checks were carried out for various conditions including uncertainties in the TOI/TOA material depth and cross-section errors, as well as the influence of different charge selections. The systematic errors associated with these uncertainties in each ratio are summed in quadrature, as shown in Table 1.

We first verified the uncertainty due to charge selection. This uncertainty is especially important in the N/O ratio measurement because of a non-negligible amount of contamination migrating from the adjacent elements C and O, which are 5–6 times more abundant than N. The greatest contributor to the uncertainty arising from this contamination is the element-dependent charge resolution. By varying the charge resolution of each element by 10% in Monte Carlo simulation, uncertainties in the abundance ratio measurement were determined to be 7% and 1% for N/O and other ratios, respectively. We further checked the results with different fit methods by using Gaussian convoluted Landau distribution. The results agree well, differing by much less than the statistical error. The same was found to hold true for the other ratios.

Next we examined the systematic effect resulting from theoretical uncertainties in the atmospheric (TOA) and instrument (TOI) corrections. An error of about 2% as quoted in Webber et al. (1990) in the calculation of the total cross section leads to 0.2% and 0.1% systematic uncertainties for N/O and the other ratio measurements, respectively. The fragmentation cross-section values from the method described in Section 3.5 differ from those reported in the literature by up to 30%. The TOI and TOA correction factor for N/O measurement is ∼45%, so an uncertainty of 15% is assigned here, making this the major source of uncertainty. The same estimates were also applied to the other ratios.

Last is the material depth of the CREAM systems located above the SCD, which varies with the trajectory of each incident particle. The effect of the dispersion of the material distribution is included as a TOI column density error. Effects from atmospheric overburden variations due to altitude changes during the flight are also included in the TOA column density error. Resulting systematic uncertainties are 3% and 1% for N/O and the other ratios, respectively.

5. DISCUSSION

The results for relative abundance ratios for C, N, O, Ne, Mg, Si, and Fe, as shown in Figure 7, extend to high energies in the TeV/nucleon region, providing more statistically significant data in that range than previously published.

For the primary-to-primary elements (C/O, Ne/O, Mg/O, Si/O, and Fe/O in Figures 7(a) and (c)–(f), respectively) the results are consistent within uncertainties with previous measurements from CRN, HEAO, and CREAM-1, and indicate that the ratios are independent of energy over the region explored. The persistence of the trend is expected because the dependence of escape path lengths on energy is thought to be independent of charge for primary elements.

For the ratio of nitrogen-to-oxygen, our result is in an energy range where the ratio may flatten out from a steep decline, as shown in Figure 7(b). This suggests a cosmic nitrogen abundance composed of both primary and secondary sources. The secondary component does have an energy dependence, while the primary does not and thus the ratio converges to a constant value at high energy. The result is in agreement with CRN and CREAM-2 measurements (Swordy et al. 1990; Ahn et al. 2009).

The GCRS abundance ratios were obtained from the abundances at the top of the atmosphere correcting for the Galactic propagation effect. The correction matrix is calculated using the GALPROP program (Strong et al. 2007). The plain diffusion model was used with a diffusion coefficient 2.28×10^{28} cm^2 s^{-1} at a reference rigidity of 3 GV (Ptuskin et al. 2006). We used $\delta = 0.6$, obtained from the B/C measurement with the CREAM-I detector (Ahn et al. 2008), and a modulation parameter of 600 MV. Uncertainty from the contribution of secondary nitrogen in the measurement of the source abundance ratio N/O is small because the secondary contribution is relatively small in the high-energy region of $E > 500$ GeV/nucleon. The source abundance ratio N/O obtained is $0.054 \pm 0.013 \pm 0.009^{+0.010}_{-0.017}$, where the first and second errors are statistical and systematic, respectively, and the last errors result from different choices of the escape parameter (0.5–0.7), representing the uncertainty on this. The solid line in Figure 7(b) is the N/O ratio curve calculated by GALPROP with the obtained source abundance ratio, while the gray colored region indicates its statistical error range. The dashed and dotted lines represent a boundary of uncertainty on $\delta = 0.5$ and 0.7, respectively. This result is in good agreement with previous measurements

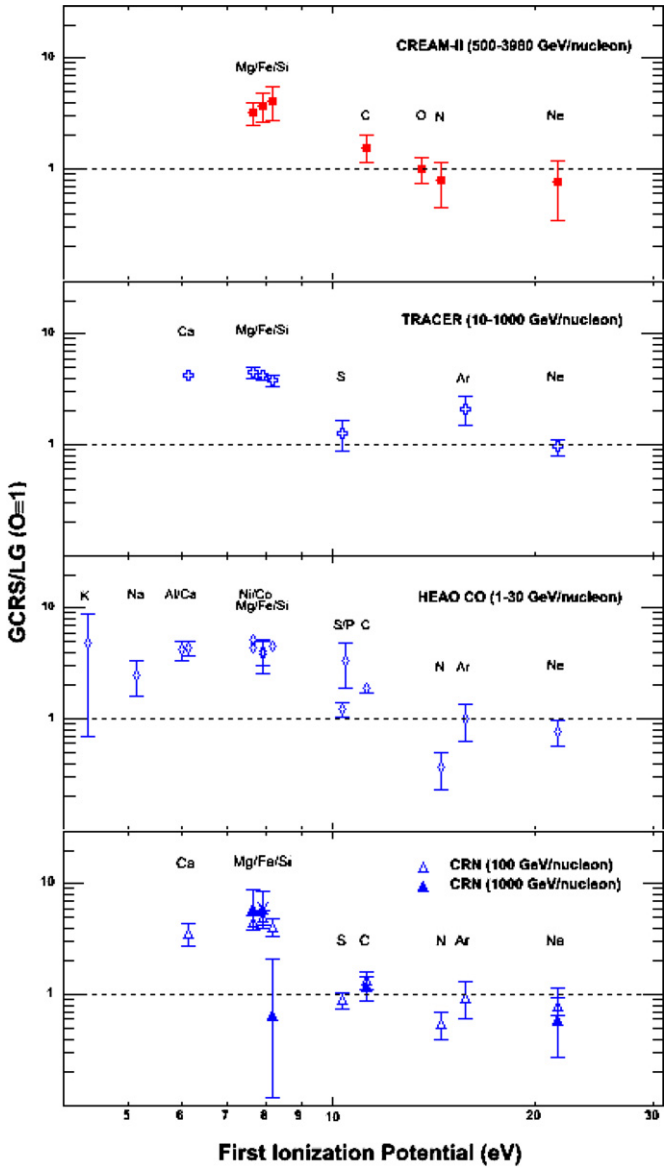

Figure 8. Ratio of the cosmic-ray source abundances to LG abundances as a function of the FIP of the elements. CREAM-II results are compared to those of TRACER, HEAO, and CRN.

(A color version of this figure is available in the online journal.)

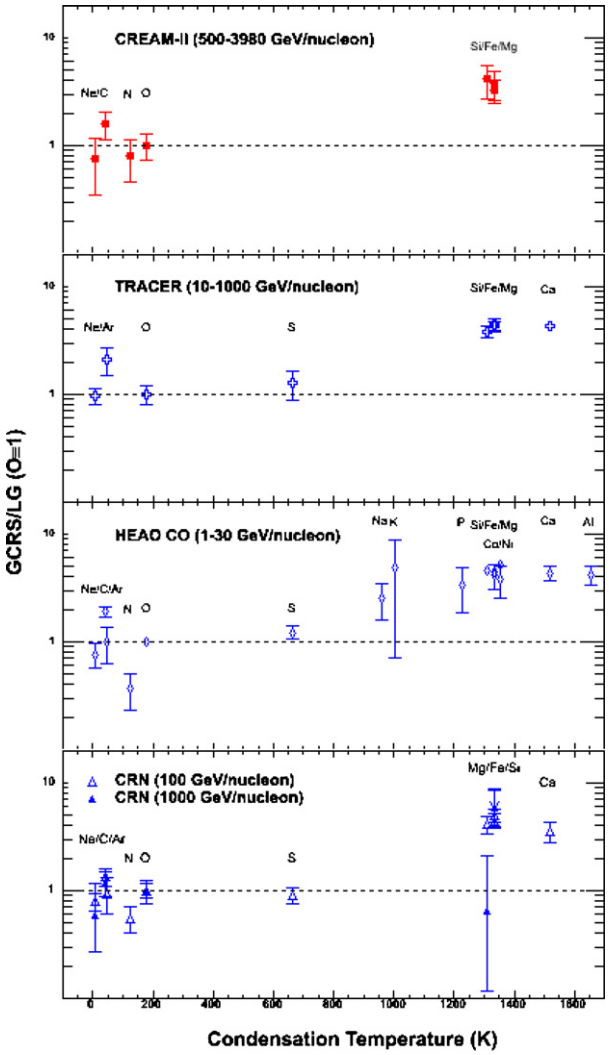

Figure 9. Ratio of the cosmic-ray source abundances to LG abundances as a function of the condensation temperature of the elements. CREAM-II results are compared to those of TRACER, HEAO, and CRN.

(A color version of this figure is available in the online journal.)

(Engelmann et al. 1990; Swordy et al. 1990; Ahn et al. 2008, 2009).

The ratios of GCRS abundances to LG abundances were also calculated for C, N, Ne, Mg, Si, and Fe, with respect to O. These are shown as a function of the FIP of the elements in Figure 8, and also as a function of the condensation temperature (T_c) (Lodders 2003) in Figure 9. Note that FIP and volatility of these elements are highly correlated. The data show the same trend seen in other measurements (Müller et al. 1991; Engelmann et al. 1990; Ave et al. 2009), namely that the cosmic-ray source abundances at large ionization potential in the FIP model or volatile elements in the volatility model, beyond about 8–9 eV, are suppressed compared to their LG abundances.

Figure 10 shows the ratio of measured GCRS abundances to the abundances consisting of a mixture of 80% SS composition (Lodders 2003) and 20% MSO material (Woosley & Heger 2007) as a function of atomic mass. In this figure, elements are divided into refractory ($T_c > 11{,}000$) and volatile groups ($T_c <$

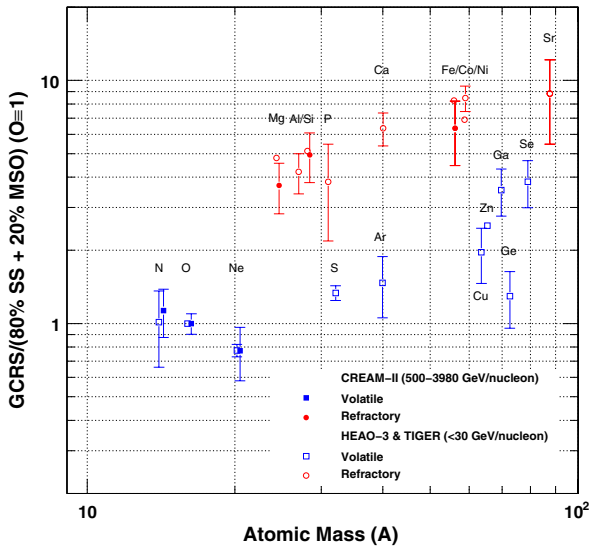

Figure 10. Ratio of the cosmic-ray source abundances to a mixture of 80% SS and 20% MSO. CREAM-II results are compared to those of HEAO and TIGER.

(A color version of this figure is available in the online journal.)

11,000). As seen in other measurements (TIGER and HEAO) in a lower energy range, the same trends of a good separation between the two groups and a power law as a function of atomic mass are seen in the CREAM-II data in the ∼TeV/nucleon range.

6. CONCLUSION

We determined the relative elemental abundances of high-energy cosmic rays using CREAM-II flight data. Particle energy was measured using a sampling tungsten/scintillating-fiber calorimeter, while charge was identified precisely with a dual-layer SCD installed for CREAM-II. The measured relative abundances of cosmic rays from carbon to silicon above 500 GeV/nucleon were found to be in good agreement with earlier measurements at lower energies. The source abundance of N/O was found to be $0.054 \pm 0.013 \pm 0.009^{+0.010}_{-0.017}$. This value is also in good agreement with a recent CREAM-I measurement using a different instrument configuration. The cosmic-ray source abundances at large ionization potential or large volatility are suppressed compared to their LG abundances, confirming a trend seen in low-energy and solar cosmic rays. Furthermore, CREAM data are found to agree with the ordering of elements in terms of the ratio of a GCRS mixture model with 80% SS composition and 20% MSO material. It confirms that a substantial fraction of MSO material is required in the ∼TeV/nucleon region.

The work reported in this paper was supported in the U.S. by NASA grants NNX08AC11G, NNX08AC15G, NNX08AC16G and their predecessor grants, in Korea by the Creative Research Initiatives (RCMST) of MEST/NRF and in Italy by INFN. The authors acknowledge NASA/WFF for provision and operation of flight support systems; Art Ruitberg, Suong Le, and Curtis Dunsmore of NASA/GSFC, and Carlos Urdiales of Southwest Research Institute for assistance with HV design and potting; CERN for provision of excellent accelerator beams; the Fermi National Accelerator Lab Thin Films Group for high-quality polishing and aluminization of optical elements; and Columbia Scientific Ballooning Facility, National Science Foundation's Office of Polar Programs, and Raytheon Polar Services Company for outstanding support of launch, flight and recovery operations in Antarctica.

REFERENCES

Ahn, H. S., et al. 2007, Nucl. Instrum. Methods Phys. Res. A, 579, 1034
Ahn, H. S., et al. 2008, Astropart. Phys., 30, 133
Ahn, H. S., et al. 2009, ApJ, 707, 593
Ahn, H. S., et al. 2010, ApJ, 714, L89
Ave, M., Boyle, P. J., Höppner, C., Marshall, J., & Müller, D. 2009, ApJ, 697, 106
Engelmann, J. J., et al. 1990, A&A, 233, 96
Garcia-Munoz, M., Simpson, J. A., Guzik, T. G., Wefel, J. P., & Margolis, S. H. 1987, ApJS, 64, 269
Juliusson, E., Meyer, P., & Mueller, D. 1972, Phys. Rev. Lett., 29, 445
Lodders, K. 2003, ApJ, 591, 1220
Marrocchesi, P. S., et al. 2004, Nucl. Instrum. Methods Phys. Res. A, 535, 143
Meyer, J. P., Drury, L. O., & Ellison, D. C. 1997, ApJ, 487, 182
Müller, D., Swordy, S. P., Meyer, P., L'Heureux, J., & Grunsfeld, 1991, ApJ, 374, 356
Müller, D., et al. 2005, Proc. 29th ICRC (Pune), 3, 89
Nam, S., et al. 2007, IEEE Trans. Nucl. Sci., 54, 1743
Olson, D. L., Berman, B. L., Greiner, D. E., Heckman, H. H., Lindstrom, P. J., & Crawford, H. J. 1983, Phys. Rev. C, 28, 1602
Park, N. H., et al. 2006, J. Korean Phys. Soc., 49, 815
Park, I. H., et al. 2007, Nucl. Instrum. Methods Phys. Res. A, 570, 286
Ptuskin, V. S., Jones, F. C., & Ormes, J. F. 1996, ApJ, 465, 972
Ptuskin, V. S., Moskalenko, I. V., Jones, F. C., Strong, A. W., & Zirakashvili, V. N. 2006, ApJ, 642, 902
Putze, A., Derome, L., Maurin, D., & Bu'enerd, M. 2008, Proc. 30th ICRC (Mérida), 4, 613
Rauch, B. F., et al. 2009, ApJ, 697, 2083
Seo, E. S., et al. 2008, Adv. Space Res., 42, 1656
Silberberg, R., & Tsao, C. H. 2004, in High-Energy Astrophysics,Vol. 1, ed. M. S. Longair (2nd ed.; Cambridge: Cambridge Univ. Press), 136
Smith, L. H., Buffington, A., Smoot, D. F., Alvarez, L. W., & Wahlig, M. A. 1973, ApJ, 180, 987
Strong, A. W., Moskalenko, I. V., & Ptuskin, V. S. 2007, Ann. Rev. Nucl. Part. Sci., 57, 285
Swordy, S. P., L'Heureux, J., Meyer, P., & Müller, D. 1993, ApJ, 403, 685
Swordy, S. P., Mueller, D., Meyer, P., L'Heureux, J., & Grunsfeld, J. M. 1990, ApJ, 349, 625
Webber, W. R., Kish, J. C., & Schrier, D. A. 1990, Phys. Rev. C, 41, 520
Woosley, S. E., & Heger, A. 2007, Phys. Rep., 442, 269
Yanasak, N., et al. 2001, ApJ, 563, 768